

JET SIGNATURES IN THE SPECTRA OF ACCRETING BLACK HOLES

MICHAEL O' RIORDAN^{1†}, ASAF PE'ER¹, JONATHAN C. MCKINNEY²

Draft version May 19, 2022

ABSTRACT

Jets are observed as radio emission in active galactic nuclei (AGN) and during the low/hard state in X-ray binaries (XRBs), but their contribution at higher frequencies has been uncertain. We study the dynamics of jets in XRBs using the general-relativistic magnetohydrodynamic (GRMHD) code **HARM**. We calculate the high-energy spectra and variability properties using a general-relativistic radiative transport code based on **grmonty**. We find the following signatures of jet emission (i) a significant γ -ray peak above $\sim 10^{22}$ Hz, (ii) a break in the optical/UV spectrum, with a change from $\nu L_\nu \sim \nu^0$ to $\nu L_\nu \sim \nu$, followed by another break at higher frequencies where the spectrum roughly returns to $\nu L_\nu \sim \nu^0$, and (iii) a pronounced synchrotron peak below $\sim 10^{15}$ Hz indicates that all higher energy emission originates in the jet. We investigate the variability during a large-scale magnetic field inversion in which the Blandford-Znajek (BZ) jet is quenched and a new transient is launched by the reconnecting field. The ratio of the γ -rays to X-rays changes from $L_\gamma/L_X > 1$ in the BZ jet to $L_\gamma/L_X < 1$ in the transient. We also find short timescale (\sim few ms) X-ray and γ -ray variability in the steady BZ jet, which we attribute to the effects of QPOs resulting from instabilities at the jet-disk interface.

1. INTRODUCTION

Jets are observed in a wide range of accreting black hole systems, from stellar-mass black holes in X-ray binaries (XRBs), to supermassive black holes in active galactic nuclei (AGN). It is widely accepted that jets are responsible for the radio emission observed both in AGN and during the low/hard state in XRBs (see e.g., Remillard & McClintock 2006; Fender 2010), however the role of jets in producing high-energy emission has typically relied upon one-zone or similar idealized models. In particular, there is no consensus regarding the origin of the X-ray component in the low/hard state in XRBs. It has long been argued that inverse Compton emission from the inner regions of the disk can significantly contribute to the X-ray spectrum (e.g., Titarchuk 1994; Magdziarz & Zdziarski 1995; Gierlinski et al. 1997; Esin et al. 1997, 2001; Poutanen 1998; Cadolle Bel et al. 2006; Yuan et al. 2007; Narayan & McClintock 2008; Niedźwiecki et al. 2012, 2014; Qiao & Liu 2015). While X-rays are expected from the disk, it is also possible that the X-rays are produced by jets (e.g., Mirabel & Rodríguez 1994; Markoff et al. 2001, 2003, 2005; Falcke et al. 2004; Bosch-Ramon et al. 2006; Kaiser 2006; Gupta et al. 2006; Kylafis et al. 2008; Maitra et al. 2009; Pe'er & Casella 2009; Pe'er & Markoff 2012; Markoff et al. 2015). This latter view has largely been motivated by the observed correlation between the radio and X-rays in the low/hard state (Corbel et al. 2000, 2003; Gallo et al. 2003). The relative importance of the disk and jet in generating the X-rays is still the subject of active research. Breaking this degeneracy is important for developing an understanding of jets and of the disk-jet connection in XRBs and other sources.

While radio observations provide a wealth of evidence for the existence of jets in AGN and XRBs, there is little

direct evidence of the conditions required for jets to form at all. The fact that jets exist in such a wide range of systems has led to the suggestion that their creation and dynamics should be governed by ingredients common to these systems. Models of jet launching therefore involve accreting plasma, magnetic fields, and the extraction of rotational energy either from a black hole (Blandford & Znajek 1977), or from the accretion disk itself (Blandford & Payne 1982).

Livio et al. (1999) argued that the BZ mechanism will not operate efficiently in standard “thin disks” (Shakura & Sunyaev 1973; Novikov & Thorne 1973) due to the fact that the magnetic flux at the horizon can not be significantly larger than that of the inner disk. Narayan et al. (2003) predicted that, if the accretion flow drags in a strong poloidal magnetic field to the black hole, the magnetic pressure will disrupt further axisymmetric accretion. They suggested that such a “magnetically arrested disk” (MAD) could be very efficient at converting the rest-mass energy of the fluid into heat, radiation, and mechanical/magnetic energy. Their MAD model relies on the key assumption that thin disks can drag magnetic fields to the horizon. Recent work by Tchekhovskoy et al. (2011) showed that the Blandford-Znajek (BZ) mechanism can efficiently power relativistic jets, provided enough magnetic flux accumulates near the black hole.

A different class of accretion flow models, which readily advect magnetic fields towards the black hole, are the so-called “advection-dominated accretion flows” (ADAFs) (Narayan & Yi 1994, 1995a,b; Abramowicz et al. 1995; Narayan & McClintock 2008; Yuan & Narayan 2014). Avara et al. (2015), with the inclusion of results from McKinney et al. (2012), showed that the BZ mechanism produces much more powerful jets in MAD ADAFs than in MAD thin disks.

A subclass of ADAFs, known as “radiatively inefficient accretion flows” (RIAFs), have been used extensively to model low luminosity systems such as the low/hard state

[†]michael_oriordan@umail.ucc.ie

¹ Physics Department, University College Cork, Cork, Ireland

² Department of Physics and Joint Space-Science Institute, University of Maryland, College Park, MD 20742, USA

in XRBs (see e.g., Narayan & McClintock 2008; Yuan & Narayan 2014). Here, low luminosity means that $L \ll L_{\text{Edd}}$, where L_{Edd} is the Eddington luminosity. The defining feature of RIAFs is that the cooling time of a fluid element is much longer than the time required for the fluid element to be accreted onto the black hole. These flows are geometrically thick, optically thin, and collisionless. Due to the fact that the electrons and ions are collisionally decoupled, they are likely to be at different temperatures, although the details of the electron thermodynamics in these systems are still being developed (Ressler et al. 2015).

The equations of general-relativistic magnetohydrodynamics (GRMHD) describe accreting systems in which the radiation is dynamically unimportant i.e. RIAFs. In the past decade, global GRMHD simulations (Gammie et al. 2003; McKinney & Gammie 2004) have greatly improved our understanding of accretion physics and jet launching. In particular, recent numerical simulations of MADs (Tchekhovskoy et al. 2011; McKinney et al. 2012) have demonstrated the launching of highly efficient jets by the BZ mechanism; we will refer to these jets as “BZ jets”. These simulations show that the BZ jet efficiency (defined as the energy extracted versus energy lost to the black hole) in MADs can be > 100 per cent. This means that more energy flows out of the black hole than flows in, which can only be achieved by extracting rotational energy from the black hole.

While these GRMHD simulations give much information about the fluid dynamics and possible jet launching mechanisms, the results can not be directly tested by comparing with observational data. To bridge this gap between theory and observations, in recent years, there has been wide interest in adding radiation to these simulations. Including radiation is necessary both for calculating the observational signatures, and for extending the simulations to regimes where the radiation becomes dynamically important i.e., where $L \gtrsim 10^{-2} L_{\text{Edd}}$ (Dibi et al. 2012).

Broadly speaking, there are two main approaches to treating the radiation. The first involves evolving the radiation field self-consistently with the matter, and is mainly used to calculate the effects of radiation on the fluid dynamics. This approach is employed in the general relativistic radiation magnetohydrodynamics (GR-RMHD) codes **KORAL** (Sądowski et al. 2013), **HARMRAD** (McKinney et al. 2014), and **bhlight** (Ryan et al. 2015). **KORAL** and **HARMRAD** treat the radiation as a separate fluid and close the fluid equations using the M1 closure (Levermore 1984), in which the radiation field is assumed to be isotropic in some frame (not necessarily the fluid frame). This approach is formally accurate at high optical depths, however fails to capture the frequency dependence required for Compton scattering, and the angular dependence expected at lower optical depths. **bhlight** solves the GRMHD equations using a direct Monte Carlo solution of the radiative transport equation. This approach has the advantage that the frequency and angular dependences of the radiation field can be included, however, since it involves tracking photons individually, it is limited to a regime in which radiative effects play a sub-dominant but non-negligible role on the dynamics. **bhlight** has been optimized for calculating the effects of radiation on the dynamical evolution, and so the spectral

resolution at low and high frequencies (which have little effect on the dynamics) is limited.

The second method involves calculating the radiation field in a post-processing step, using the fluid data as input. Examples of general-relativistic radiative transport codes which employ a post-processing approach include **grmonty** (Dolence et al. 2009), **ASTRORAY** (Shcherbakov & Huang 2011), **GRay** (Chan et al. 2013), and **HEROIC** (Zhu et al. 2015; Narayan et al. 2015). Since the fluid data is supplied by an external code, the post-processing algorithms can be optimized for calculating spectra and images. The disadvantage of this approach is that it is only applicable in regimes in which the radiation is dynamically unimportant. These codes have been used by many authors to calculate the observational signatures of low luminosity systems in which the radiation pressure can be neglected (e.g. Mościbrodzka et al. 2009; Mościbrodzka & Falcke 2013; Mościbrodzka et al. 2014; Chan et al. 2009, 2015b,a; Shcherbakov et al. 2012; Shcherbakov & McKinney 2013). These works mainly focussed on reproducing the spectra and variability properties of Sgr A*, and place important constraints on quantities such as the black hole spin, proton-to-electron temperature ratio, and inclination angle. The constraints placed on the proton-to-electron temperature ratio could also be relevant for the low/hard state in XRBs.

We use a similar post-processing approach, with a radiative transport code based on the freely available **grmonty**. Here, we are interested in identifying the observational signatures of jet emission in XRBs. Since our goal is to study jets, we use GRMHD simulations of RIAFs, supplied by the **HARM** code, as input for our post-processing calculation. We perform our radiative transport calculations for both MAD and non-MAD RIAFs (the latter are called SANE in Narayan et al. 2012, where SANE stands for “standard and normal evolution”), and find significant differences in the resulting spectra. Furthermore, we make a distinction between jet and disk emission, and keep track of whether or not photons had some interaction (emission or scattering) with the jet before escaping the system. This allows us to determine the jet contribution to the spectrum, and identify unique observational signatures of jets.

Our paper is organised as follows. In Section 2 we briefly describe our 3D GRMHD simulations and radiative transport code. In Section 3 we present our results, showing the observational jet signatures and variability properties of the jet and disk emission. In Section 4 we discuss our findings and summarize our main results.

2. MODEL

2.1. GRMHD simulation

We are interested in jets and so we focus on RIAFs, since these are likely necessary for jet launching by the BZ mechanism (Livio et al. 1999; Meier 2001; Avara et al. 2015). In this case, radiation is dynamically unimportant and the evolution is well described by standard GRMHD codes. We use the **HARM** code (Gammie et al. 2003; McKinney & Gammie 2004), which evolves the GRMHD equations using a conservative, shock-capturing scheme. For our MAD model, we choose the fiducial model, A0.94BfN40, from McKinney et al. (2012) in which the magnetic field has saturated near the black hole. In this

magnetically choked accretion flow (MCAF), the black hole magnetosphere compresses the inflow such that it becomes geometrically thin and the standard magneto-rotational instability (MRI) is suppressed. The jet power in the BZ model is given by (Blandford & Znajek 1977; Tchekhovskoy et al. 2010; Yuan & Narayan 2014)

$$P_{\text{BZ}} = \frac{\kappa}{4\pi c} \Phi^2 \Omega_H^2 \quad (1)$$

where Φ is the magnetic flux threading the horizon, $\Omega_H = ac/2r_H$ is the angular velocity of the horizon, and $\kappa \approx 0.05$ is a dimensionless coefficient which depends weakly on the magnetic field geometry. The horizon radius, r_H , is given by $r_H = (1 + \sqrt{1 - a^2})r_g$, where a is the dimensionless black-hole spin, $r_g = GM/c^2$, and M is the mass of the black hole. Thus, the highly magnetized state over most of the horizon (see Figure 1), and large black-hole spin ($a = 0.9375$), are optimal for the BZ mechanism to generate powerful, relativistic jets (Tchekhovskoy et al. 2011; McKinney et al. 2012).

The initial mass distribution is an isentropic hydro-equilibrium torus (Fishbone & Moncrief 1976; Gammie et al. 2003) with the inner edge at $r = 10r_g$ and pressure maximum at $r = 100r_g$. The magnetic field has poloidal geometry with multiple loops of alternating polarity for inducing magnetic field inversion/annihilation. These field inversions quench and relaunch magnetically dominated BZ jets (see Section 3.2).

The jet forms as a highly magnetized, low density funnel region along the spin axis of the black hole. In Figure 1 we show snapshots of the electron number density n , and magnitude of the magnetic field B , at $t = 26548r_g/c$. These plots are scaled to the low/hard state in XRBs, with a black hole mass $M = 10M_\odot$ and accretion rate $\dot{M} = 3 \times 10^{-7} \dot{M}_{\text{Edd}}$, where \dot{M}_{Edd} is the Eddington accretion rate defined as $\dot{M}_{\text{Edd}} = L_{\text{Edd}} / (0.1c^2)$ (see e.g., Narayan & McClintock 2008). The inner $r \lesssim 10r_g$ of the disk is compressed by the black hole magnetosphere. The density enhancements in the jet are due to instabilities at the jet-disk interface (see Section 3.2). The horizon and funnel regions are both highly magnetized. We use the ratio of the magnetic and rest-mass energy densities to define the jet, i.e. where $b^2/\rho c^2 \geq \xi$, for some constant ξ . Here, ρ is the rest mass density of the gas, and $b^2 = b^\mu b_\mu$, where b^μ is the magnetic field four-vector. The precise value of ξ is somewhat arbitrary and depends on the particular simulation. We find that $\xi = 0.5$ gives a reasonable distinction between the jet and disk in our simulations.

It is also possible to distinguish between the jet, disk, and magnetized wind. The wind can be defined roughly by the condition that $b^2/\rho c^2 < \xi$ and $\beta_p < 2$ (McKinney et al. 2012), where $\beta_p = p_{\text{gas}}/p_{\text{mag}}$ is the ratio of gas and magnetic pressures. The disk then corresponds to the region with $b^2/\rho c^2 < \xi$ and $\beta_p \geq 2$. In our MAD simulation, the disk is very thick and maintains approximately uniform density to the boundary, so the wind is limited to a small part of the fluid at the jet-disk interface. Therefore, for our purposes, we choose only to distinguish between the disk and funnel regions.

The HARM code (and similar GRMHD codes) fail if the rest-mass density ρ , or the internal energy density u become too small in comparison with b^2 . This is avoided by

using density ‘‘floors’’, which effectively inject mass into the system in regions where these floors are activated. The internal energy is chosen to enforce $u/\rho c^2 \leq 50$, then ρ is chosen with the conditions that $b^2/\rho c^2 \leq 50$ and $b^2/u \leq 10^3$. These floors are mainly activated in the highly-magnetized, low-density funnel region. Mass injection is expected to occur at the stagnation surface separating the inflowing and outflowing plasma (Globus & Levinson 2013), however, GRMHD simulations which self-consistently account for this injection have not yet been developed. Therefore, as a first approximation, we include the mass injected via the density floors in our radiative transport calculations.

The simulation runs for a total time of $t_f = 26548 r_g/c$ and reaches a quasi-steady state by time $t \approx 8000 r_g/c$. A snapshot of the fluid data is saved every $\Delta t = 4r_g/c$. Modified spherical coordinates are used, with resolution $N_r \times N_\theta \times N_\phi = 272 \times 128 \times 256$. This simulation is the highest resolution, longest duration 3D simulation of a MAD configuration to date. The grid extends to a maximum radius of $R_{\text{out}} = 26000 r_g$. In order to focus on the dynamics at small radii while avoiding numerical reflections off the outer boundary, the resolution is concentrated near the black hole, with a transition at $r = 500 r_g$ to a much sparser grid (see McKinney et al. 2012, for details). We limit our analysis to the inner $r = 200 r_g$, which corresponds to 194 cells in the radial direction. Coordinate singularities along the poles can cause further numerical difficulties and so we exclude cells near the poles from our radiative transport calculations. This can be seen as an excised region along the z -axis in Figure 1.

As previously mentioned, the disk in our MAD simulation is very thick. The jet is collimated by pressure support from the thick disk, and remains nearly cylindrical out to the boundary at $r = 200 r_g$. For comparison, we checked our results against the A0.99N100 model from McKinney et al. (2012). This model is a MAD RIAF and is qualitatively similar to the fiducial model, however, the disk is thinner. We find similar spectra in both cases, indicating that our results are not just peculiarities of the very thick disk.

For our SANE model, we use the dipole model of McKinney & Blandford (2009). In this simulation, a MAD state does not develop and the accretion is driven by the MRI. In Figure 2 we show snapshots of the electron number density and magnetic field, at $t = 4000 r_g/c$, using the same parameters as in Figure 1. The black-hole magnetosphere does not disrupt the inner accretion flow in this case, and so the inner disk is geometrically thicker and less dense than in the MAD simulation. While the jet efficiency in our MAD simulation is > 100 per cent, the corresponding efficiency in our SANE simulation is only about 1 per cent, even with a large black-hole spin of $a = 0.92$.

The initial disk torus has inner edge at $r = 6r_g$, pressure maximum at $r = 12r_g$, and contains a single magnetic field loop. The simulation runs for a total time of $t_f = 5000 r_g/c$ and reaches a quasi-steady state by time $t \approx 3000 r_g/c$. The grid resolution is $N_r \times N_\theta \times N_\phi = 256 \times 128 \times 32$, and warps to follow the disk at small radii and the jet at large radii. The outer boundary is located at $R_{\text{out}} = 1000 r_g$. Again, we

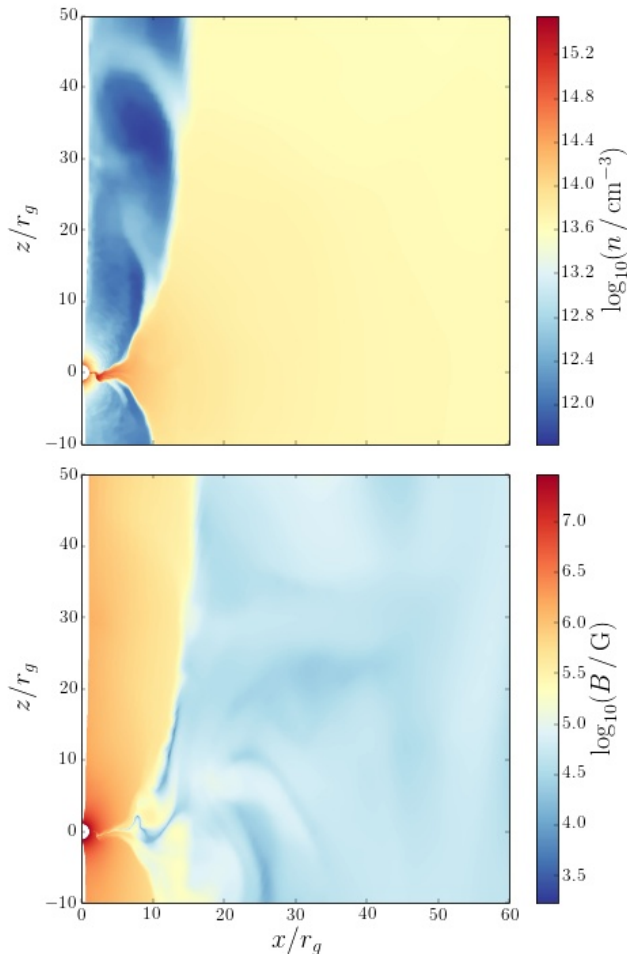


FIG. 1.— Electron number density and magnetic field strength close to the black hole, at $t = 26548r_g/c$, in our MAD model. The inner $r \lesssim 10r_g$ of the disk is compressed by the black hole magnetosphere. The disk itself is geometrically thick, with approximately uniform density out to the boundary. The jet is visible as a lower density funnel region. The density enhancements in the jet are the result of QPOs driven by instabilities at the jet-disk interface. The jet region is highly magnetized, with $B \sim 10^6 - 10^7$ G.

limit our calculations to the inner $r = 200r_g$ and excise cells near the poles. We distinguish between the jet and disk using the same condition on $b^2/\rho c^2$ as in the MAD case.

2.2. Radiative transport

We calculate the spectra and variability properties of the low/hard state in XRBs using a general relativistic radiative transport code based on the freely available `grmonty` (Dolence et al. 2009). This code uses a post-processing approach for calculating the spectra and relies on an external fluid model to supply the rest-mass density ρ , internal energy density u , fluid four-velocity u^μ , and magnetic field four-vector b^μ , at every point in the grid. We interpolate these quantities to arbitrary points as needed. We modify the original code to work with general 3D HARM data as input, and to allow for different temperature prescriptions in the disk and in the jet.

The spectra are calculated assuming synchrotron emission, self-absorption, and Compton scattering from a thermal distribution of relativistic electrons. We define the dimensionless electron temperature $\Theta \equiv kT_e/mc^2$,

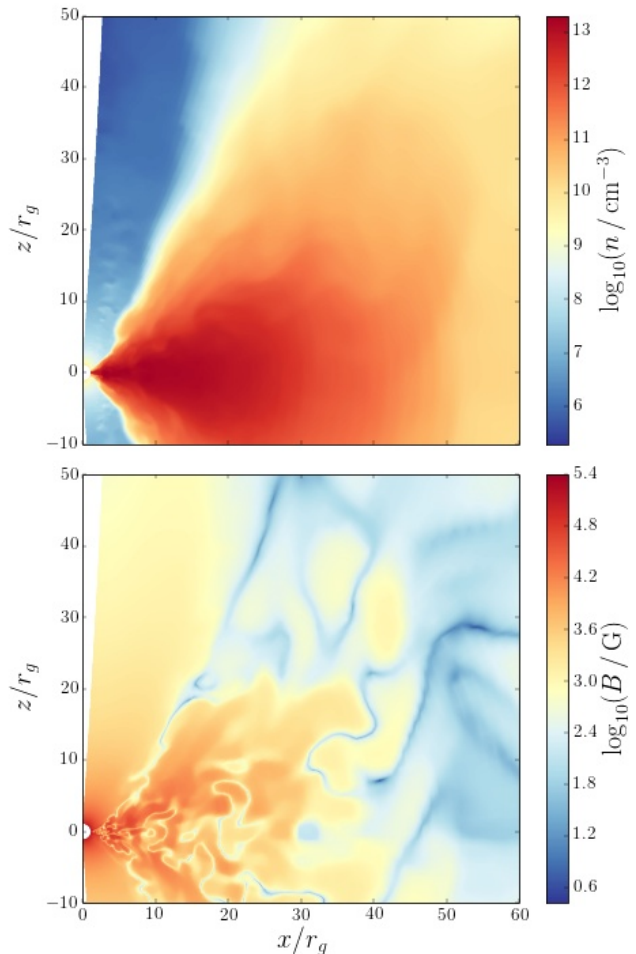


FIG. 2.— Electron number density and magnetic field strength close to the black hole, at $t = 4000r_g/c$, in our SANE model. The inner disk is geometrically thicker and less dense than in the MAD case. The magnetic field in the jet is also significantly weaker in this model.

where k is Boltzmann’s constant, and m is the electron mass. The distribution function for relativistic electrons at temperature Θ is then

$$\frac{dn}{d\gamma} = \frac{n}{\Theta} \frac{\gamma^2 \beta}{K_2(\Theta^{-1})} \exp\left(-\frac{\gamma}{\Theta}\right) \quad (2)$$

where n is the number density of electrons, $\gamma = (1 - \beta^2)^{-1/2}$ is the electron Lorentz factor, β is the electron speed in the fluid frame, and K_2 is the modified Bessel function of the second kind. We neglect any radiative cooling of the electrons and so the electron distribution function is determined, at every point in the grid, by the local fluid properties. We use the following emissivity for thermal synchrotron emission, valid for $\Theta \gtrsim 0.5$ (see Dolence et al. 2009)

$$j_\nu = \frac{\sqrt{2}\pi e^2 n \nu_s}{3c K_2(\Theta^{-1})} \left(X^{1/2} + 2^{11/12} X^{1/6}\right)^2 \exp(-X^{1/3}) \quad (3a)$$

$$X \equiv \frac{\nu}{\nu_s} \quad (3b)$$

$$\nu_s \equiv \frac{2}{9} \left(\frac{eB}{2\pi mc}\right) \Theta^2 \sin \theta \quad (3c)$$

where e is the electron charge, B is the magnetic field strength, and θ is the angle between the photon wave vector and the magnetic field. The absorption coefficient is calculated as

$$\alpha_{\nu,a} = \frac{j_\nu}{B_\nu} \quad (4)$$

where B_ν is the Planck function. The extinction coefficient for Compton scattering from a distribution of relativistic electrons is given by

$$\alpha_{\nu,s} = n\sigma_h \quad (5)$$

where σ_h is the ‘‘hot cross section’’ defined as

$$\sigma_h \equiv \frac{1}{n} \int d^3p \frac{dn}{d^3p} (1 - \mu\beta)\sigma_{\text{KN}} \quad (6)$$

Here, p is the electron four-momentum, $d^3p = dp_1 dp_2 dp_3$, and μ is the cosine of the angle between the electron momentum and photon momentum in the fluid frame. The Klein-Nishina cross section, σ_{KN} , is

$$\sigma_{\text{KN}} = \sigma_T \frac{3}{4\epsilon^2} \left(2 + \frac{\epsilon^2(1+\epsilon)}{(1+2\epsilon)^2} + \frac{\epsilon^2 - 2\epsilon - 2}{2\epsilon} \log(1+2\epsilon) \right) \quad (7)$$

where σ_T is the Thomson cross section, and $\epsilon = e'\gamma(1 - \mu\beta)$ is the photon energy (in units of mc^2) in the electron rest frame, and e' is the photon energy in the fluid frame. We use the thermal distribution in equation (2) when calculating the hot cross section (6). The scattering calculation samples the Klein-Nishina differential cross section

$$\frac{2\pi}{\sigma_T} \frac{d\sigma_{\text{KN}}}{d\epsilon_s} = \frac{1}{\epsilon_s} \left(\frac{\epsilon}{\epsilon_s} + \frac{\epsilon_s}{\epsilon} - 1 + \cos^2\theta_s \right) \quad (8)$$

where ϵ_s is the energy of the scattered photon, and θ_s is the scattering angle in the electron frame.

The details of the electron thermodynamics in RIAFs have not been determined. A common approach is to assume that the electron temperature is some constant fraction of the proton temperature, and to use this ratio as a free parameter (Mościbrodzka et al. 2009). Although more sophisticated models are being developed (Ressler et al. 2015), there are still many parameters whose values are unknown. Because of these uncertainties, we use the simple assumption of a constant proton-to-electron temperature ratio T_p/T_e . However, due to differences in density, magnetization, etc., the heating mechanisms could be significantly different in the disk and in the jet, so we vary this temperature ratio independently in these regions (Chan et al. 2015b; Ressler et al. 2015). We define a proton-to-electron temperature ratio \mathcal{R}_d in the disk where $b^2/\rho c^2 < 0.5$, and a ratio \mathcal{R}_j in the jet where $b^2/\rho c^2 \geq 0.5$.

Introducing radiation breaks the scale-free nature of the GRMHD data. We set the length and time scales by specifying the black hole mass M . The appropriate scales are then the gravitational radius, r_g , and the light crossing time, $t_g = r_g/c$. The mass/energy unit is not set by M because the fluid mass is $\ll M$. We set this unit by prescribing the mass accretion rate \dot{M} . Using these, the HARM data can be scaled to a particular system, for example, the mass density is set as $\rho = (\dot{M}t_g/r_g^3)\tilde{\rho}$, where $\tilde{\rho}$ is the dimensionless mass density given by the

Model	\mathcal{R}_d	\mathcal{R}_j
1	3	3
2	10	10
3	30	30
4	3	10
5	3	30
6	10	30
7	10	3
8	30	3
9	30	10

TABLE 1
LIST OF MAD MODEL PROTON-TO-ELECTRON TEMPERATURE RATIOS.

HARM code. For our purposes, we choose $M = 10M_\odot$ and $\dot{M} = 3 \times 10^{-7}\dot{M}_{\text{Edd}}$.

We track $\sim 10^8$ photons to an outer radial boundary of $r = 200r_g$. The choice of this boundary is discussed in Section 2.1 and has little effect on the results as most of the high-energy emission originates close to the black hole. By tracking photons individually, we can unambiguously determine the jet contribution to the spectrum.

For computational simplicity, we use a ‘‘fast light’’ approximation in which the fluid data is treated as time-independent during the radiative transport calculation. This approximation may break down in regions where the light crossing time is comparable to the dynamical time, however, we perform our post-processing calculation only after the fluid simulation has reached a quasi-steady state and so we expect this to be a reasonable approach. Furthermore, Shcherbakov et al. (2012) performed both time-independent and fully time-dependent radiative transport calculations in the context of Sgr A*, and found good agreement in most cases.

3. RESULTS

3.1. Jet signatures

For our MAD model, we calculate spectra for the nine temperature models listed in Table 1. Since differences in density and magnetization in the disk and jet can lead to different cooling rates for the electrons in these regions, we allow for different temperature ratios, \mathcal{R}_d and \mathcal{R}_j , in the disk and magnetized funnel. The values of these ratios depend on poorly understood electron thermodynamics. However, assuming that (i) the dissipation of turbulence mainly heats the protons, (ii) the cooling time for the electrons is shorter than that of the protons, and (iii) the electron cooling time is shorter than the timescale for significant energy exchange between the electrons and protons, we expect these temperature ratios to be greater than unity (Yuan & Narayan 2014; Chan et al. 2015b). Furthermore, because of the similarities between AGN and the low/hard state in XRBs, we assume that the physics of electron heating and cooling is the same across these systems. We therefore choose a range of values of \mathcal{R}_d and \mathcal{R}_j motivated by fitting to Sgr A* and M87, since these are the only sources whose spectra have been fitted to constrain these parameters (Mościbrodzka et al. 2009; Mościbrodzka & Falcke 2013; Mościbrodzka et al. 2014; Chan et al. 2015b; Mościbrodzka et al. 2015).

We choose three models with $\mathcal{R}_d = \mathcal{R}_j$, three with $\mathcal{R}_d < \mathcal{R}_j$, and three with $\mathcal{R}_d > \mathcal{R}_j$, shown in Figures 3, 4, and 5, respectively. In each Figure, the distinc-

tion between the jet and disk contributions is defined such that the “jet interaction” (short dashes) component corresponds to the contribution from photons which either originated in the jet or scattered in the jet before escaping. The “disk only” (long dashes) component corresponds to photons which originated in the disk and escaped without scattering in the jet (possibly scattering in the disk before leaving the system).

In Figure 3 we show the spectra calculated with $\mathcal{R}_d = \mathcal{R}_j$. The middle panel shows the spectrum calculated with $(\mathcal{R}_d, \mathcal{R}_j) = (10, 10)$. This spectrum qualitatively captures the main spectral features present in most models, which we describe below. Both the “disk only” and “jet interaction” components have three peaks. The peak in the “disk only” component at $\sim 10^{15}$ Hz is due to synchrotron emission from the disk, while the two higher peaks at $\sim 10^{19}$ Hz and $\sim 10^{22}$ Hz result from single and double synchrotron self-Compton, respectively. The peak in the “jet interaction” component at $\sim 10^{18}$ Hz is due to synchrotron emission from the jet, while the peak at $\sim 10^{22}$ Hz corresponds to synchrotron photons from the jet which scattered once in the disk before escaping. The peak at $\sim 10^{23}$ Hz is due to single scattering in the jet. In all models with $\mathcal{R}_d = \mathcal{R}_j$, the disk dominates in the optical, while the jet contributes significantly to the X-rays and γ -rays. The disk contributes to the hard X-rays in models with $\mathcal{R}_d < 30$. In these models, the disk emission peaks around 10^{22} Hz, and decays rapidly above this. The emission decays since the photons have been scattered up to the same temperature as the electrons in the disk. In what follows, we will refer to this frequency as the “saturation frequency”, ν_{sat} .

It is interesting to note that, although all these models have $\mathcal{R}_d = \mathcal{R}_j$, there are differences in the resulting spectra. This is due to the strong dependence of the scattering on the electron temperature. The synchrotron peak depends on the temperature as $(\nu j\nu)_{\text{syn}} \sim \Theta^2$, while the inverse Compton peak goes like $(\nu j\nu)_{\text{IC}} \sim y(\nu j\nu)_{\text{syn}} \sim \Theta^4$. Here, y is the Compton y parameter given by $y = 16\Theta^2\tau$ (Rybicki & Lightman 1979), and τ is the optical depth. We have assumed that the fluid is optically thin, and that the electrons are ultrarelativistic, $\gamma \gg 1$, and have a thermal distribution.

In Figure 4 we show spectra calculated with $\mathcal{R}_d < \mathcal{R}_j$. The features in the “disk only” component are similar to those in Figure 3, with a synchrotron peak around $\sim 10^{15}$ Hz, and two higher energy peaks due to single and double synchrotron self-Compton. The “jet interaction” component shows a synchrotron peak at $\sim 10^{18}$ Hz, and a peak at 10^{22} Hz corresponding to photons which originated in the jet and scattered once in the disk before escaping. The disk dominates most of the spectra in this case. The high-energy γ -ray peak, present in models with $\mathcal{R}_d = \mathcal{R}_j$, is absent or obscured by the hotter disk contribution.

In Figure 5 we show spectra calculated with $\mathcal{R}_d > \mathcal{R}_j$. In this case, the jet dominates most of the spectrum, with a small contribution from the disk around the optical band. The peak around $\sim 10^{15}$ Hz is due to synchrotron from the disk, while the peak at $\sim 10^{19}$ Hz is synchrotron emission from the jet. The third peak, at $\sim 10^{21}$ Hz, again corresponds to photons which were emitted in the jet and scattered once in the disk. The peak in the γ -rays

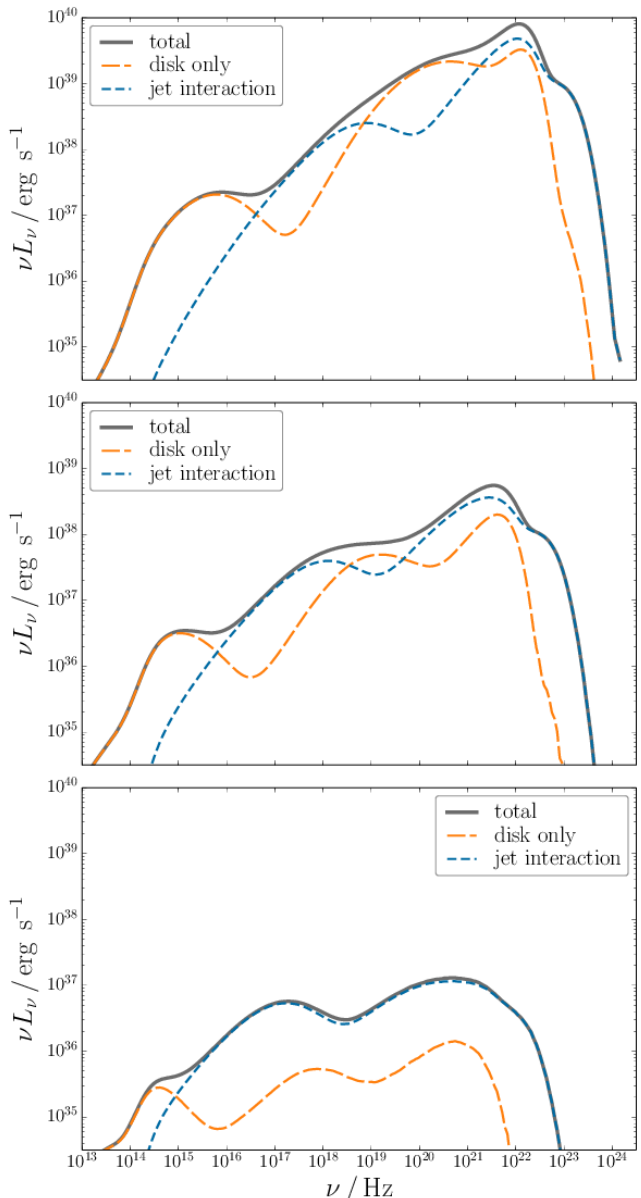


FIG. 3.— MAD model spectra with $\mathcal{R}_d = \mathcal{R}_j$. From top to bottom, these were calculated with $(\mathcal{R}_d, \mathcal{R}_j) = (3, 3), (10, 10), (30, 30)$, respectively. The disk contribution dominates mainly around 10^{15} Hz, while the jet contributes significantly in the X-rays and γ -rays.

around 10^{23} Hz is due to scattering in the jet.

The locations of the synchrotron and saturation peaks provide a wealth of information about the fluid properties in the jet and in the disk. The ratio of the jet and disk synchrotron peak frequencies depends on the temperatures and magnetic fields as $\nu_{\text{syn},j}/\nu_{\text{syn},d} \sim \Theta_j^2 B_j / \Theta_d^2 B_d$. The saturation frequency is simply proportional to the electron temperature, $\nu_{\text{sat}} \sim \Theta$. Therefore, the ratio of jet and disk magnetic fields can be estimated from the spectra as

$$\frac{B_j}{B_d} \sim \left(\frac{\nu_{\text{syn},j}}{\nu_{\text{syn},d}} \right) \left(\frac{\nu_{\text{sat},d}}{\nu_{\text{sat},j}} \right)^2 \quad (9)$$

For example, the top panel of Figure 5 shows $\nu_{\text{sat},d}/\nu_{\text{sat},j} \sim 1/30$ and $\nu_{\text{syn},j}/\nu_{\text{syn},d} \sim 10^4$, which cor-

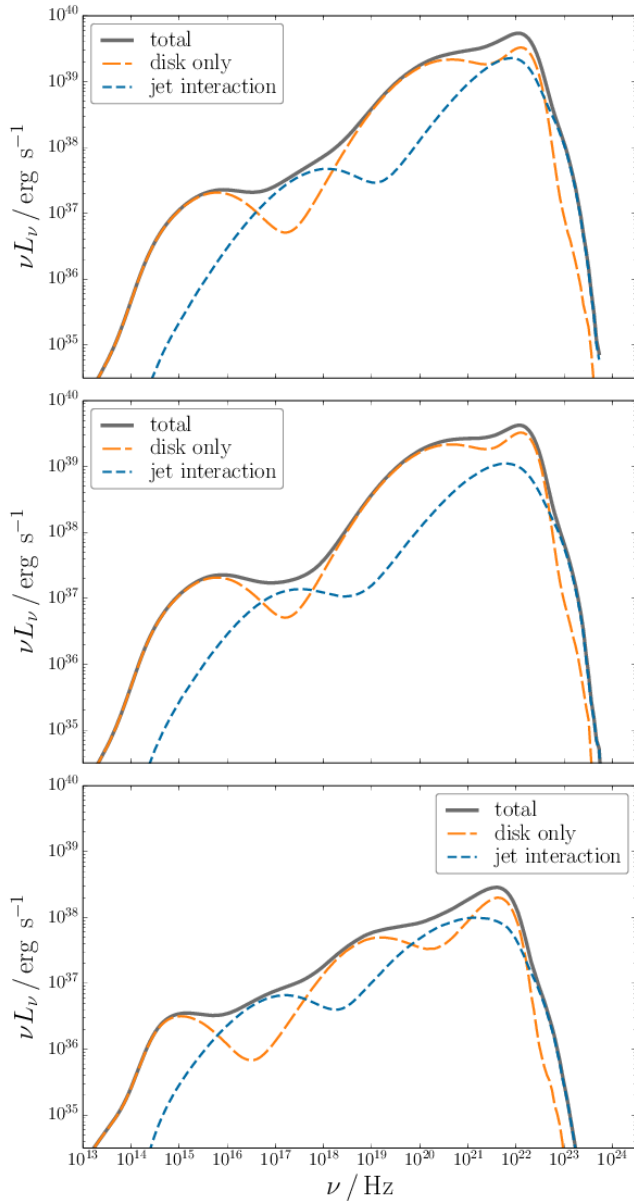


FIG. 4.— Same as Figure 3 but for models with $\mathcal{R}_d < \mathcal{R}_j$. From top to bottom $(\mathcal{R}_d, \mathcal{R}_j) = (3, 10), (3, 30), (10, 30)$, respectively. The disk dominates the spectra at all wavelengths in this case. However, there are frequencies where the jet contributes significantly.

responds to a magnetic field ratio of $B_j/B_d \sim 10$. This analysis is independent of the temperature model, however, we have used the fact that the jet in our simulation is only mildly relativistic.

While separating the spectrum into jet and disk components is useful for identifying their contributions, in reality, this decomposition is not so straightforward. Therefore, we are interested in identifying signatures of jet emission in the composite spectrum.

In all our MAD calculations, the highest energy emission is produced by inverse Compton scattering of synchrotron photons. Therefore, the electron temperature sets an upper limit on the high energy emission. In all models with $\mathcal{R}_d \geq \mathcal{R}_j$ (Figures 3 and 5) the jet electrons are one or two orders of magnitude hotter than those in

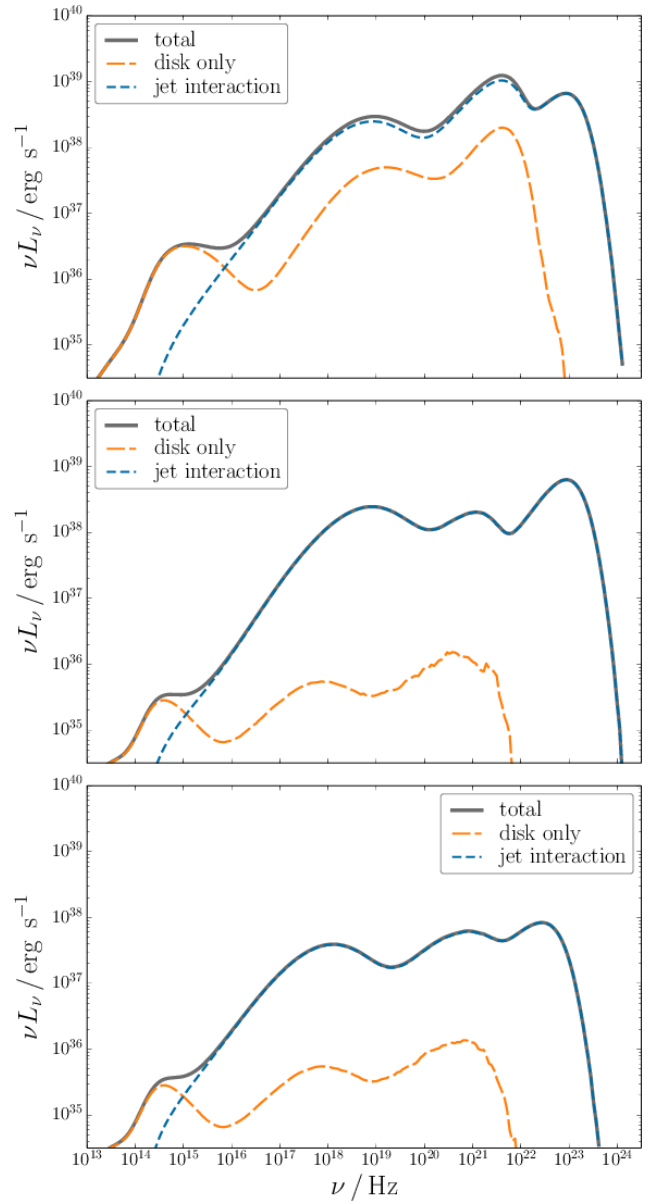


FIG. 5.— Same as Figure 3 but for models with $\mathcal{R}_d > \mathcal{R}_j$. From top to bottom $(\mathcal{R}_d, \mathcal{R}_j) = (10, 3), (30, 3), (30, 10)$, respectively. The jet dominates everything above $\sim 10^{16}$ Hz.

the disk. Therefore, we expect the highest energy emission to come from the jet. This is clearly visible in the spectra as a γ -ray peak in the jet component around $\sim 10^{23}$ Hz, well above the highest energy disk contribution. This feature is absent in disk-dominated spectra, i.e., those with $\mathcal{R}_d < \mathcal{R}_j$ (see Figure 4). We conclude that this high-energy feature could be a good indicator of jet emission.

Another possible signature of jet emission occurs in regions where the spectra change from disk to jet dominated. The overlapping jet and disk components tend to smooth out parts of the spectrum which would otherwise be much steeper. Most of the spectra from our MAD simulation show roughly flat ($\nu L_\nu \sim \nu^0$) regions, followed by a break where the spectrum changes to $\nu L_\nu \sim \nu$. This can be seen clearly in the spectra in Figure 5, with breaks around $\sim 10^{15}$ Hz. There is a second break in the

spectrum around $\sim 10^{18}$ Hz, where it returns roughly to $\nu L_\nu \sim \nu^0$. This second break is followed by “wiggles” in spectrum, with variations in the luminosity of a factor of a few. These features are less clear in models where the spectra are almost completely dominated by disk emission ($\mathcal{R}_d < \mathcal{R}_j$). The breaks are due to the combined effect of the jet and disk contributions, and so are a clear indication of the presence of jet emission.

For our SANE model, we use the same black hole mass and accretion rate as in our MAD calculations. Since we are interested in signatures of jets, we choose temperature models which show some jet contribution, i.e., those with $\mathcal{R}_d > \mathcal{R}_j$. In Figure 6 we show spectra calculated with $(\mathcal{R}_d, \mathcal{R}_j) = (10, 3)$, $(30, 3)$, and $(30, 10)$. These spectra are significantly different to those from the MAD model. The synchrotron emission from the disk peaks in the IR, as opposed to in the optical/UV in the MAD case. Compton scattering is also sub-dominant. These differences can be attributed to the fact that the inner disk in the MAD model is denser and hotter than the disk in the SANE model.

The middle panel of Figure 6 shows the spectrum calculated with $\mathcal{R}_d = 30$, and $\mathcal{R}_j = 3$. The peak at $\sim 10^{13}$ Hz is due to synchrotron emission from the disk, while synchrotron from the jet dominates at all frequencies above this. The bottom panel shows the spectrum with $\mathcal{R}_d = 30$, and $\mathcal{R}_j = 10$, and is qualitatively similar, with a synchrotron peak around $\sim 10^{13}$ Hz, and synchrotron from the jet dominating at all higher frequencies. We can enhance the contribution from scattering in the disk by increasing the temperature of the disk electrons. This is shown in the top panel of Figure 6, with $\mathcal{R}_d = 10$, and $\mathcal{R}_j = 3$. There is still a significant contribution from the jet at higher frequencies in this case. These results imply that a pronounced peak at about $\sim 10^{13}$ Hz indicates that all higher energy emission originates from the jet. However, at the same accretion rate, the MAD accretion flow is much more luminous than the SANE case. For example, comparing the synchrotron peaks in the top panels of Figures 5 and 6, we see that the disk is roughly 7 orders of magnitude more luminous in the MAD case. This may limit the observability of any jet signatures deduced from Figure 6.

The synchrotron peak scales with the accretion rate as $(\nu j_\nu)_{\text{syn}} \sim n\Theta^2 B^2 \sim \dot{M}^2$. We can therefore increase the total luminosity by choosing higher accretion rates. In Figure 7 we show spectra from our SANE model, calculated with $(\mathcal{R}_d, \mathcal{R}_j) = (30, 3)$ and accretion rates of $3 \times 10^{-5} \dot{M}_{\text{Edd}}$ (top panel) and $3 \times 10^{-4} \dot{M}_{\text{Edd}}$ (bottom panel). These spectra show a pronounced synchrotron peak from the disk at or below $\sim 10^{15}$ Hz. In the model with $\dot{M} = 3 \times 10^{-5} \dot{M}_{\text{Edd}}$, the jet component dominates at all frequencies above the disk synchrotron peak, while in the model with $\dot{M} = 3 \times 10^{-4} \dot{M}_{\text{Edd}}$, the jet and disk components are comparable and so the distinction between them is not clear. We conclude that a pronounced synchrotron peak below $\sim 10^{15}$ Hz, which can be attributed to the disk, indicates that any higher-energy features must be due to emission from the jet.

In Figure 8 we show spectra calculated with the same accretion rates as in Figure 7, but with $(\mathcal{R}_d, \mathcal{R}_j) = (10, 3)$. In this case, there is a peak at $\sim 10^{15}$ Hz due to

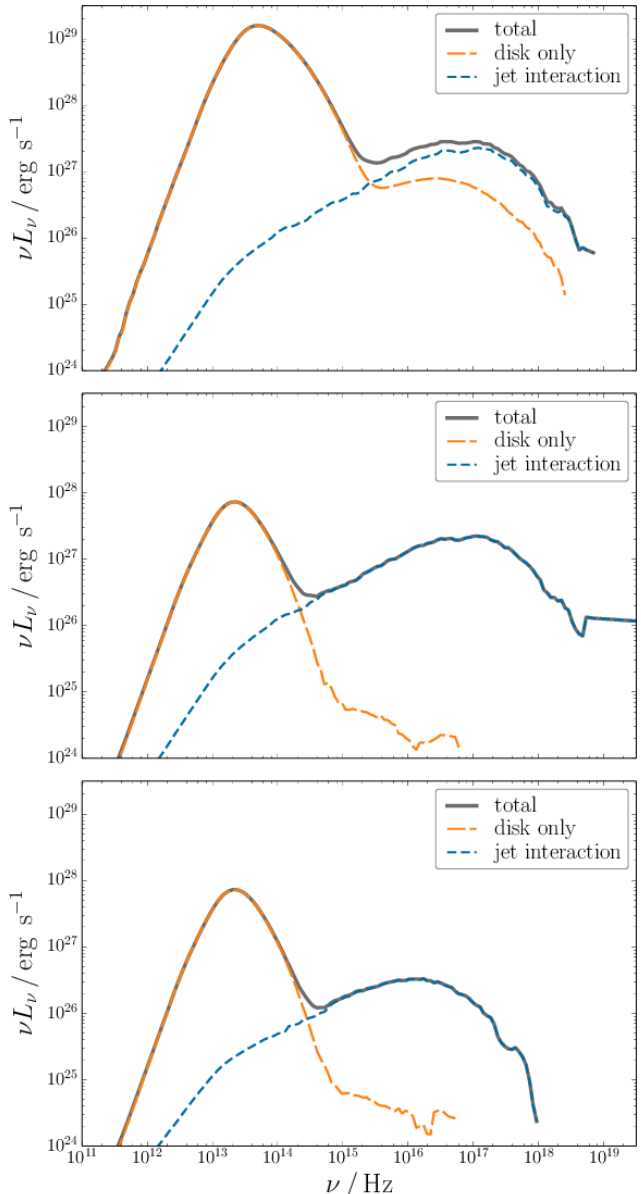


FIG. 6.— SANE model spectra. From top to bottom, these were calculated with $(\mathcal{R}_d, \mathcal{R}_j) = (10, 3)$, $(30, 3)$, $(30, 10)$, respectively. The disk synchrotron peaks around $\sim 10^{13}$ Hz, while the high-energy emission is dominated by the jet. Some of the high-energy emission is noisy due to poor photon statistics.

synchrotron emission from the disk, while the rest of the spectrum up to $\sim 10^{21}$ Hz is dominated by synchrotron self-Compton from the disk. Interestingly, although the disk component dominates most of the spectrum, there is significant γ -ray emission $\gtrsim 10^{22}$ Hz. As in the MAD case, this is due to scattering in the jet and is located at higher frequencies than the disk saturation frequency, i.e., above where the disk emission decays. Therefore, this is a robust signature of jet emission which is independent of whether the accretion flow is MAD or SANE.

3.2. Jet-disk correlated variability

In this Section, we investigate jet variability in our MAD model, and so choose a temperature model which produces significant jet emission. In what follows we set

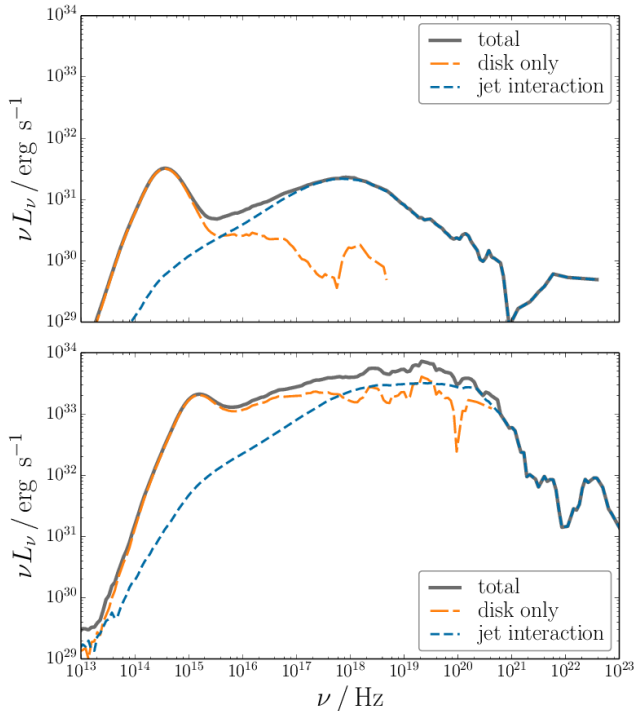


FIG. 7.— SANE model spectra calculated with $(\mathcal{R}_d, \mathcal{R}_j) = (30, 3)$. The top panel shows the spectrum with $\dot{M} = 3 \times 10^{-5} \dot{M}_{\text{Edd}}$, while the bottom panel has $\dot{M} = 3 \times 10^{-4} \dot{M}_{\text{Edd}}$. In both models, the highest energy γ -ray emission is dominated by the jet. In models where the disk synchrotron peaks below $\sim 10^{15}$ Hz, all emission above this peak is completely dominated by the jet. In models where this synchrotron peak is at or above $\sim 10^{15}$ Hz, the jet may still have a significant contribution in the X-rays, however the distinction between the jet and disk components is less clear. The higher energy emission is noisy due to poor photon statistics.

$\mathcal{R}_d = 10$, and $\mathcal{R}_j = 3$. The lightcurves in Figure 9 show variability at 10^{15} Hz, 10^{19} Hz, and 10^{23} Hz, during a quasi-steady period of the MAD simulation (i.e., well after $t \approx 8000 r_g/c$). The main contributions at these frequencies are synchrotron from the disk, synchrotron from the jet, and scattering from the jet, respectively. In Figure 10, we show the power spectral density (PSD) of these curves. The PSDs show fast, correlated variability in the optical, X-ray and γ -ray lightcurves, with a period of $T \approx 35 r_g/c$. We attribute this variability to the effects of quasi-periodic oscillations (QPOs) on the jet. The QPOs result from instabilities at the jet-disk interface and can be seen in Figure 1 as density enhancements in the funnel region (for a discussion of the effects of QPOs on the dynamics of the jet see McKinney et al. 2012). The observable effects of these QPOs were discussed in the context of Sgr A* in Shcherbakov & McKinney (2013), however, the effects on the jet emission were neglected. In order to achieve a temporal resolution of $\Delta t = 4 r_g/c$, we reduced the number of photons in our radiative transport calculation to $\sim 10^6$. Our lightcurves are therefore quite noisy. We leave a more complete analysis of this jet-QPO variability to future work.

The initial magnetic field in our MAD model contains multiple poloidal field loops, with adjacent field loops having opposite polarity. The accretion of these loops causes a large-scale magnetic field inversion which

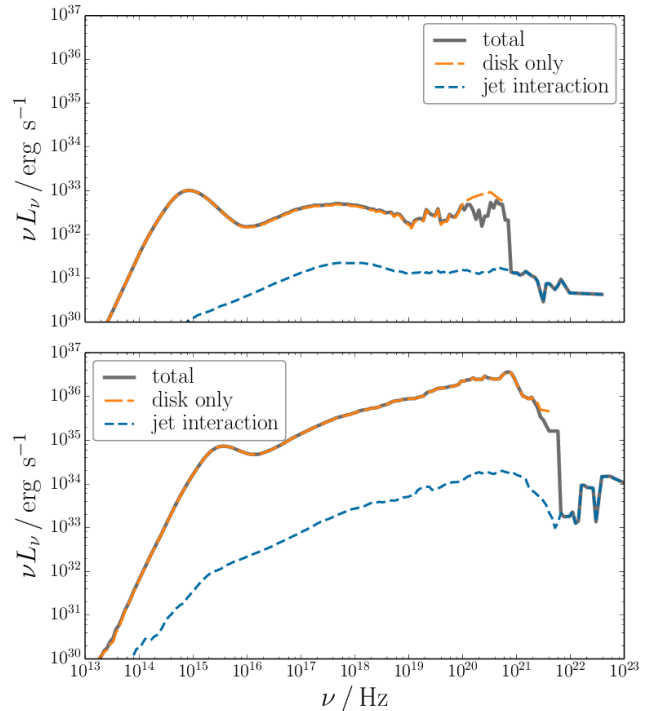


FIG. 8.— SANE model spectra calculated with $(\mathcal{R}_d, \mathcal{R}_j) = (10, 3)$. The top panel shows the spectrum with $\dot{M} = 3 \times 10^{-5} \dot{M}_{\text{Edd}}$, while the bottom panel has $\dot{M} = 3 \times 10^{-4} \dot{M}_{\text{Edd}}$. Synchrotron emission and scattering from the disk dominate most of the spectrum. Similar to the MAD case, the high-energy γ -ray emission at $\sim 10^{22}$ Hz is due to scattering in the jet.

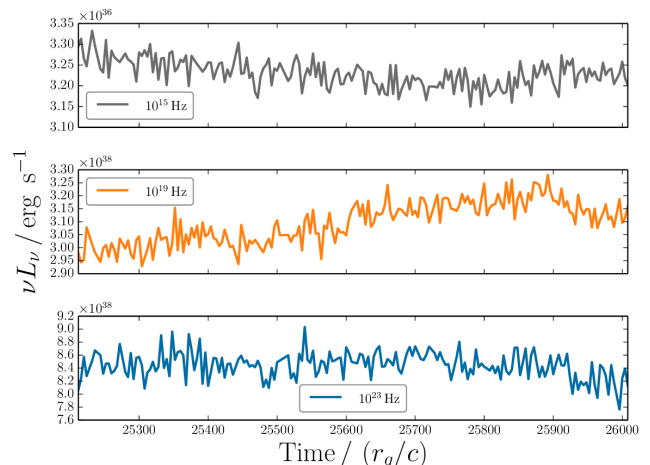


FIG. 9.— Lightcurves at 10^{15} Hz, 10^{19} Hz, and 10^{23} Hz corresponding to synchrotron from the disk, synchrotron from the jet, and scattering from the jet, respectively. These were calculated with $\mathcal{R}_d = 10$, $\mathcal{R}_j = 3$.

quenches the BZ jet (Dexter et al. 2014). This process might be responsible for the observed state transitions in XRBs (Igumenshchev 2009). In Figure 11, we show the evolution of the optical, X-rays, and γ -rays during such an inversion. In the initial BZ jet, the ratio of the γ -ray to X-ray luminosities is $L_\gamma/L_X > 1$. The BZ jet is quenched during the field inversion and a new transient jet is launched by reconnection of the MAD field close to the BH (Dexter et al. 2014). This transient

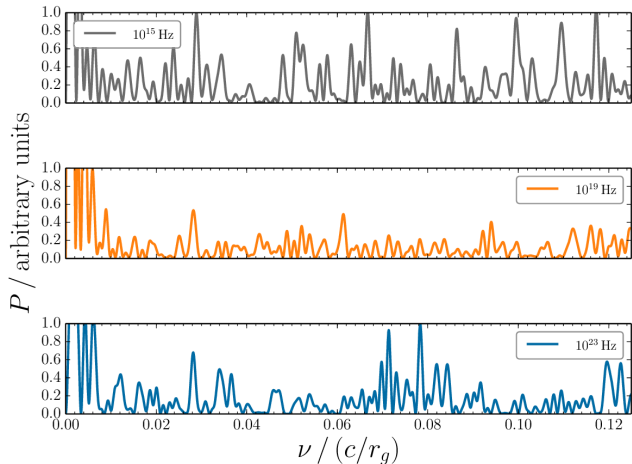


FIG. 10.— PSDs for the lightcurves in Figure 9. The peaks at $\nu \approx 0.028 (c/r_g)$ show correlated, short-timescale variability with a period of $T \approx 35 r_g/c$.

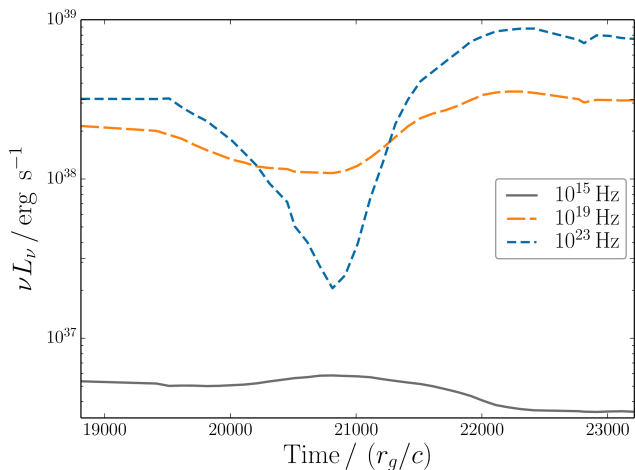


FIG. 11.— Optical, X-ray, and γ -ray variability during a global magnetic field inversion. These lightcurves were calculated with $\mathcal{R}_d = 10$, $\mathcal{R}_j = 3$. The γ -ray luminosity varies by nearly two orders of magnitude, and the ratio of the γ -ray to X-ray luminosities, L_γ/L_X , varies such that $L_\gamma/L_X > 1$ in the steady BZ jet and $L_\gamma/L_X < 1$ in the transient jet.

jet has $L_\gamma/L_X < 1$. After the inversion, the disk returns to a MAD state and the BZ jet is re-launched with $L_\gamma/L_X > 1$. During this process (a timescale of $\sim 2000 r_g/c \sim 0.1$ s), the γ -ray luminosity varies by nearly two orders of magnitude while the X-rays vary by a factor of a few. There is a small increase in optical emission from the disk, peaking around the minimum of the γ -ray and X-ray emission from the jet. The re-launched BZ jet is significantly more luminous in the γ -rays and X-rays, while the disk is less luminous after the outburst.

4. DISCUSSION

In this work, we calculated the spectrum of a RIAF in the context of the low/hard state in XRBs, with the goal of identifying high-energy signatures of jets in these systems. We investigated both MAD and SANE RIAFs, and find the following observational signatures of jet emission: (i) A significant peak in the γ -rays at $\sim 10^{23}$ Hz. (ii) A break in the optical/UV spectrum

where it transitions from disk to jet dominated, changing from $\nu L_\nu \sim \nu^0$ at lower frequencies to $\nu L_\nu \sim \nu$ at higher frequencies. This is followed by a second break around $\sim 10^{18}$ Hz, where the spectrum roughly returns to $\nu L_\nu \sim \nu^0$, with “wiggles” in the luminosity of a factor of a few. (iii) A pronounced peak below $\sim 10^{15}$ Hz indicates that jet emission dominates at all frequencies above this. These signatures are present across a range of proton-to-electron temperature ratios.

Comparing the spectra in Figures 5 and 8, we find that spectra from our MAD model are almost completely jet dominated while those from our SANE model are dominated by the disk. In particular, the X-rays are produced by synchrotron self-Compton from the disk in our SANE model, while jet synchrotron emission dominates the X-rays in our MAD model. Our results suggest that the two competing models of X-ray production in XRBs, namely the synchrotron and synchrotron self-Compton models, are realised separately in MAD and SANE accretion flows, respectively. Therefore, an investigation of the observational signatures of MAD vs SANE systems could provide valuable insights into breaking the degeneracy between these X-ray models. We will study these observational signatures further in a future work.

In our MAD model, we find short timescale (\sim few ms) variability in the X-rays and γ -rays, which we attribute to the effects of QPOs on the jet. The effects of QPOs on the jet dynamics were discussed in McKinney et al. (2012), and their effects on disk emission were discussed in Shcherbakov & McKinney (2013). Here, we extend this analysis to include the effects on jet emission. Although noisy, our results indicate that QPOs can cause variability in both X-rays and γ -rays from the jet. We leave a detailed analysis of this disk-jet connection to a future paper. Finally, we investigated the evolution of the jet and disk emission during a large-scale magnetic field inversion in which the BZ jet is quenched and a new transient jet is launched. During this process, the X-ray and γ -ray luminosities vary dramatically with $L_\gamma/L_X > 1$ in the BZ jet and $L_\gamma/L_X < 1$ in the transient outburst. This transient is qualitatively similar to those observed during state transitions in XRBs (Dexter et al. 2014).

Our analysis was carried out for a limited range of fluid models and temperature ratios, however, it is straightforward to estimate how the spectra would change with variations in n , Θ , and B . The synchrotron and inverse Compton peak frequencies scale with fluid properties as $\nu_{\text{syn}} \sim \Theta^2 B$, and $\nu_{\text{IC}} \sim \Theta^2 \nu_{\text{syn}}$, respectively. The heights of these peaks scale as $(\nu j_\nu)_{\text{syn}} \sim n \Theta^2 B^2$, and $(\nu j_\nu)_{\text{IC}} \sim y (\nu j_\nu)_{\text{syn}} \sim n \Theta^2 (\nu j_\nu)_{\text{syn}}$. The saturation frequency is proportional to the electron temperature, $\nu_{\text{sat}} \sim \Theta$. We can then scale our XRB results to AGN as follows. Assuming that the accretion rate is proportional to the black hole mass, the magnetic field, number density, and electron temperature in RIAFs vary with M as $B \sim M^{-1/2}$, $n \sim M^{-1}$, and $\Theta \sim M^0$ (see the discussion about scaling the HARM data to a particular system in Section 2.2). With these relationships, and the dependence of the spectral features on these quantities as outlined above, we can scale our results to arbitrary black hole masses.

While we can apply our results to both XRBs and

AGN, our work is limited to the study of jets launched by the BZ mechanism. In particular, it is uncertain whether the BZ mechanism powers jets in gamma-ray bursts (GRBs). For example, in the standard “fireball” model (see e.g., Mészáros 2006, and references therein), outflows are accelerated by radiation pressure instead of magnetic fields. We therefore exclude these objects from our analysis.

The most significant limitation of the current work is the assumption of a thermal distribution of electrons. This may be a reasonable assumption for the disk, however it is likely that the jet will contain a significant amount of non-thermal particles due to shocks and magnetic reconnection. Also, the “fast light” approximation,

which we use for computational efficiency, is an oversimplification since the dynamical time of the accretion disk and jet can be close to the light crossing time. We will extend this analysis to include the effects of non-thermal particles and time-dependence in a future work.

MOR is supported by the Irish Research Council by grant number GOIPG/2013/315. This research was partially supported by the European Union Seventh Framework Programme (FP7/2007-2013) under grant agreement no 618499. JCM acknowledges NASA/NSF/TCAN (NNX14AB46G), NSF/XSEDE/TACC (TG-PHY120005), and NASA/Pleiades (SMD-14-5451).

REFERENCES

- Abramowicz, M. A., Chen, X., Kato, S., Lasota, J.-P., & Regev, O. 1995, *ApJ*, 438, L37
- Avara, M. J., McKinney, J. C., & Reynolds, C. S. 2015, *ArXiv e-prints*
- Blandford, R. D. & Payne, D. G. 1982, *MNRAS*, 199, 883
- Blandford, R. D. & Znajek, R. L. 1977, *MNRAS*, 179, 433
- Bosch-Ramon, V., Romero, G. E., & Paredes, J. M. 2006, *A&A*, 447, 263
- Cadotte Bel, M., Sizun, P., Goldwurm, A., Rodriguez, J., Laurent, P., Zdziarski, A. A., Foschini, L., Goldoni, P., Gouiffès, C., Malzac, J., Jourdain, E., & Roques, J.-P. 2006, *A&A*, 446, 591
- Chan, C.-k., Liu, S., Fryer, C. L., Psaltis, D., Özel, F., Rockefeller, G., & Melia, F. 2009, *ApJ*, 701, 521
- Chan, C.-k., Psaltis, D., & Özel, F. 2013, *ApJ*, 777, 13
- Chan, C.-k., Psaltis, D., Özel, F., Medeiros, L., Marrone, D., Sądowski, A., & Narayan, R. 2015a, *ArXiv e-prints*
- Chan, C.-K., Psaltis, D., Özel, F., Narayan, R., & Sądowski, A. 2015b, *ApJ*, 799, 1
- Corbel, S., Fender, R. P., Tzioumis, A. K., Nowak, M., McIntyre, V., Durouchoux, P., & Sood, R. 2000, *A&A*, 359, 251
- Corbel, S., Nowak, M. A., Fender, R. P., Tzioumis, A. K., & Markoff, S. 2003, *A&A*, 400, 1007
- Dexter, J., McKinney, J. C., Markoff, S., & Tchekhovskoy, A. 2014, *MNRAS*, 440, 2185
- Dibi, S., Drappeau, S., Fragile, P. C., Markoff, S., & Dexter, J. 2012, *MNRAS*, 426, 1928
- Dolence, J. C., Gammie, C. F., Mościbrodzka, M., & Leung, P. K. 2009, *ApJS*, 184, 387
- Esin, A. A., McClintock, J. E., Drake, J. J., Garcia, M. R., Haswell, C. A., Hynes, R. I., & Muno, M. P. 2001, *ApJ*, 555, 483
- Esin, A. A., McClintock, J. E., & Narayan, R. 1997, *ApJ*, 489, 865
- Falcke, H., Körding, E., & Markoff, S. 2004, *A&A*, 414, 895
- Fender, R. 2010, in *Lecture Notes in Physics*, Berlin Springer Verlag, Vol. 794, Lecture Notes in Physics, Berlin Springer Verlag, ed. T. Belloni, 115
- Fishbone, L. G. & Moncrief, V. 1976, *ApJ*, 207, 962
- Gallo, E., Fender, R. P., & Pooley, G. G. 2003, *MNRAS*, 344, 60
- Gammie, C. F., McKinney, J. C., & Tóth, G. 2003, *ApJ*, 589, 444
- Gierlinski, M., Zdziarski, A. A., Done, C., Johnson, W. N., Ebisawa, K., Ueda, Y., Haardt, F., & Philips, B. F. 1997, *MNRAS*, 288, 958
- Globus, N. & Levinson, A. 2013, *Phys. Rev. D*, 88, 084046
- Gupta, S., Böttcher, M., & Dermer, C. D. 2006, *ApJ*, 644, 409
- Igumenshchev, I. V. 2009, *ApJ*, 702, L72
- Kaiser, C. R. 2006, *MNRAS*, 367, 1083
- Kylafis, N. D., Papadakis, I. E., Reig, P., Giannios, D., & Pooley, G. G. 2008, *A&A*, 489, 481
- Levermore, C. D. 1984, *J. Quant. Spec. Radiat. Transf.*, 31, 149
- Livio, M., Ogilvie, G. I., & Pringle, J. E. 1999, *ApJ*, 512, 100
- Magdziarz, P. & Zdziarski, A. A. 1995, *MNRAS*, 273, 837
- Maitra, D., Markoff, S., Brocksopp, C., Noble, M., Nowak, M., & Wilms, J. 2009, *MNRAS*, 398, 1638
- Markoff, S., Falcke, H., & Fender, R. 2001, *A&A*, 372, L25
- Markoff, S., Nowak, M., Corbel, S., Fender, R., & Falcke, H. 2003, *A&A*, 397, 645
- Markoff, S., Nowak, M., Gallo, E., Hynes, R., Wilms, J., Plotkin, R. M., Maitra, D., Silva, C. V., & Drappeau, S. 2015, *ArXiv e-prints*
- Markoff, S., Nowak, M. A., & Wilms, J. 2005, *ApJ*, 635, 1203
- McKinney, J. C. & Blandford, R. D. 2009, *MNRAS*, 394, L126
- McKinney, J. C. & Gammie, C. F. 2004, *ApJ*, 611, 977
- McKinney, J. C., Tchekhovskoy, A., & Blandford, R. D. 2012, *MNRAS*, 423, 3083
- McKinney, J. C., Tchekhovskoy, A., Sadowski, A., & Narayan, R. 2014, *MNRAS*, 441, 3177
- Meier, D. L. 2001, *ApJ*, 548, L9
- Mészáros, P. 2006, *Reports on Progress in Physics*, 69, 2259
- Mirabel, I. F. & Rodríguez, L. F. 1994, *Nature*, 371, 46
- Mościbrodzka, M. & Falcke, H. 2013, *A&A*, 559, L3
- Moscibrodzka, M., Falcke, H., & Shiokawa, H. 2015, *ArXiv e-prints*
- Mościbrodzka, M., Falcke, H., Shiokawa, H., & Gammie, C. F. 2014, *A&A*, 570, A7
- Mościbrodzka, M., Gammie, C. F., Dolence, J. C., Shiokawa, H., & Leung, P. K. 2009, *ApJ*, 706, 497
- Narayan, R., Igumenshchev, I. V., & Abramowicz, M. A. 2003, *PASJ*, 55, L69
- Narayan, R. & McClintock, J. E. 2008, *NewAR*, 51, 733
- Narayan, R., Sądowski, A., Penna, R. F., & Kulkarni, A. K. 2012, *MNRAS*, 426, 3241
- Narayan, R. & Yi, I. 1994, *ApJ*, 428, L13
- . 1995a, *ApJ*, 444, 231
- . 1995b, *ApJ*, 452, 710
- Narayan, R., Zhu, Y., Psaltis, D., & Sadowski, A. 2015, *ArXiv e-prints*
- Niedźwiecki, A., Xie, F.-G., & Stępnik, A. 2014, *MNRAS*, 443, 1733
- Niedźwiecki, A., Xie, F.-G., & Zdziarski, A. A. 2012, *MNRAS*, 420, 1195
- Novikov, I. D. & Thorne, K. S. 1973, in *Black Holes (Les Astres Occlus)*, ed. C. Dewitt & B. S. Dewitt, 343–450
- Pe’er, A. & Casella, P. 2009, *ApJ*, 699, 1919
- Pe’er, A. & Markoff, S. 2012, *ApJ*, 753, 177
- Poutanen, J. 1998, in *Theory of Black Hole Accretion Disks*, ed. M. A. Abramowicz, G. Björnsson, & J. E. Pringle, 100–+
- Qiao, E. & Liu, B. F. 2015, *MNRAS*, 448, 1099
- Remillard, R. A. & McClintock, J. E. 2006, *ARA&A*, 44, 49
- Ressler, S. M., Tchekhovskoy, A., Quataert, E., Chandra, M., & Gammie, C. F. 2015, *ArXiv e-prints*
- Ryan, G., van Eerten, H., MacFadyen, A., & Zhang, B.-B. 2015, *ApJ*, 799, 3
- Rybicki, G. B. & Lightman, A. P. 1979, *Radiative processes in astrophysics*
- Sądowski, A., Narayan, R., Tchekhovskoy, A., & Zhu, Y. 2013, *MNRAS*, 429, 3533
- Shakura, N. I. & Sunyaev, R. A. 1973, *A&A*, 24, 337
- Shcherbakov, R. V. & Huang, L. 2011, *MNRAS*, 410, 1052
- Shcherbakov, R. V. & McKinney, J. C. 2013, *ApJ*, 774, L22
- Shcherbakov, R. V., Penna, R. F., & McKinney, J. C. 2012, *ApJ*, 755, 133
- Tchekhovskoy, A., Narayan, R., & McKinney, J. C. 2010, *ApJ*, 711, 50

—, 2011, MNRAS, 418, L79

Titarchuk, L. 1994, ApJ, 434, 570

Yuan, F. & Narayan, R. 2014, ARA&A, 52, 529

Yuan, F., Zdziarski, A. A., Xue, Y., & Wu, X.-B. 2007, ApJ, 659,
541

Zhu, Y., Narayan, R., Sadowski, A., & Psaltis, D. 2015, MNRAS,
451, 1661